A systematic study of structural, magnetic and electrical properties of $(La_{1-x}Tb_x)_{2/3}Ca_{1/3}MnO_3$ perovskites

A systematic study of structural, magnetic and electrical properties of $(La_{1-x}Tb_x)_{2/3}Ca_{1/3}MnO_3$ perovskites

J Blasco, J García, J M de Teresa, M R Ibarra, P A Algarabel and
C Marquina

Instituto de Ciencia de Materiales de Aragón, Consejo Superior de Investigaciones Científicas,
Universidad de Zaragoza, 50009 Zaragoza, Spain

Abstract. A thorough study of the $(La_{1-x}Tb_x)_{2/3}Ca_{1/3}MnO_3$ series has been carried out. All of the samples have the same orthorhombic crystallographic structure. However, the magnetic, magnetoelastic and electrical properties show drastic changes with the Tb content. The decrease in the intensity of the ferromagnetic double-exchange interaction has been correlated with the increase in the Tb content and the decrease in the Mn–O–Mn bond angle, which leads to a decrease in the electron transfer between Mn 3d and O 2p orbitals. Two magnetic phases have been detected at low temperatures: an insulator spin-glass phase in samples with high Tb contents and a metallic ferromagnetic phase in samples with low Tb contents.

1. Introduction

The mixed-valence manganese perovskites $La_{1-x}A_xMnO_3$ (A = Ca, Sr, Ba) were exhaustively studied in the past [1–4]. In these series, the valence state of the manganese atom changes continuously from trivalent ($x = 0$) to tetravalent ($x = 1$) giving rise to the existence of different electrical transport properties and magnetic orderings of the Mn moments. $LaMnO_3$ is an antiferromagnetic insulator, as explained via a superexchange interaction, with $T_N = 141$ K [5, 6]. The partial replacement of La^{3+} by divalent cations (Ca, Sr or Ba) gives rise to a ferromagnetic ordering in a narrow range of concentrations [1, 4]. The highest value of T_c obtained in $La_{1-x}A_xMnO_3$ samples is reached for $x \approx 0.33$ [3]. A metallic-like behaviour is observed below T_c in these doped compounds. Ferromagnetism and metallic conduction have been explained through the double-exchange interaction [7, 8].

Recently, there has been renewed interest in the study of these mixed oxides because of the discovery of giant magnetoresistance in thin films and polycrystalline samples [9, 10]. The main interest has been focused on $La_{2/3}A_{1/3}MnO_3$ due to it having the highest Curie temperature and largest magnetoresistive effect [11]. Very recent studies have shown that the partial replacement of lanthanum with other trivalent rare-earth or related atoms causes a decrease in the Curie temperature and a large enhancement of the magnetoresistance [12–14]. Among these compounds, $La_{0.6}Y_{0.07}Ca_{0.33}MnO_3$ has aroused great interest due to the 'colossal' negative magnetoresistance $\Delta R/R \approx -10\,000\%$ with a $T_c = 160$ K [14]. In [14] the authors claim that the drop in T_c and the rise in the magnetoresistance is related to the diminution of the unit cell due to the substitution for La of a smaller ion (yttrium). Further studies of magnetoresistance on this sample at high external pressures have shown that the decrease in the unit cell produces the opposite effect: an increase in T_c and a decrease in

magnetoresistance [15] as has also been observed for $La_{1-x}Sr_xMnO_3$ perovskites [16]. In the course of our research on the yttrium-doped compound we found the existence of an anomaly in the linear thermal expansion at T_c which is suppressed by a magnetic field [17]. This work showed that charge localization brings about local distortions which are closely correlated with the magnetotransport properties in these materials. The study of $(La, RE)_{0.7}A_{0.3}MnO_3$ compounds (RE: rare earth), with the same concentration of carriers, have revealed a tight relationship between T_c and the average ionic radius of the trivalent rare earth. Consequently, a universal behaviour of $RE_{0.7}A_{0.3}MnO_3$ compounds has been proposed, the Mn–O–Mn angle being the parameter that determines the magnetic and transport properties in these compounds [12]. These results, together with the magnetovolume effects, point to a considerable coupling between the magnetism and lattice. The strong Jahn–Teller electron–phonon coupling has been proposed to play an important role in these compounds [18, 19].

In order to understand all of these results and to achieve a deeper knowledge, it is necessary to carry out systematic studies over the full series. We have chosen the $(La_{1-x}Tb_x)_{2/3}Ca_{1/3}MnO_3$ $(0 \leqslant x \leqslant 1)$ system because Tb^{3+} is a smaller ion than La^{3+} and it is possible to form solid solutions with the perovskite structure over the whole concentration range [20]. As our attempts to obtain a single phase of $Y_{2/3}Ca_{1/3}MnO_3$ were unsuccessful, resulting a mixture of the perovskite structure and the hexagonal $YMnO_3$ [21, 22], we discarded the study of the $(La_{1-x}Y_x)_{2/3}Ca_{1/3}MnO_3$ series.

We have focused our work on several points. First: the correlation between structure and macroscopic properties, i.e. what are the structural parameters which control the ferromagnetic state? Second: are the ferromagnetism and metallic conductivity correlated? Or, does a ferromagnetic insulating phase exist in these compounds with this carrier concentration as has been proposed [12]? Third: is the ferromagnetic phase transition always associated with a volume anomaly? The answers to these points can help us to solve some basic questions about the electronic features that control the giant magnetoresistance. In order to correlate minor crystallographic changes with drastic variations in the physical properties and to explore the mechanisms which drive the magnetoresistive behaviour of these materials, we have undertaken a thorough crystallographic, magnetic, electrical and magnetoelastic study. We will show that the double-exchange interaction, responsible for the ferromagnetic coupling, must be generalized to include the electron–phonon interactions and their dependence on the crystal structure. This should explain the close correlation between ferromagnetism and the metallic state in this system.

2. Experimental details

$(La_{1-x}Tb_x)_{2/3}Ca_{1/3}MnO_3$ $(x = 0, 0.04, 0.075, 0.15, 0.25, 0.33, 0.5, 0.75, 1)$ samples were prepared by using a sol–gel method in order to optimize the mixture of starting material [23]. Stoichiometric amounts of La_2O_3, Tb_4O_7, $CaCO_3$ and $MnCO_3$ with nominal purities not less than 99.99% were dissolved in nitric acid. After this, citric acid and ethylene glycol were added and the aqueous solutions were evaporated until they gave a brown gel. These gels were heated to the combustion point; the result was a fine black–brown powder. These powders were calcined overnight at 950 °C and then they were pressed at 4 kbar and sintered at 1000 °C for two days with several regrindings. Finally they were sintered at 1250 °C for eight hours. All of the samples showed monophasic x-ray diffraction patterns. All of the syntheses were performed in air in order to produce samples with stoichiometric oxygen contents [1]. The oxygen content was analysed using standard redox titration [24]. All of the samples studied in this work were stoichiometric within analytical errors.

Step-scanned powder diffraction patterns for all of the samples were collected at room

temperature using a D-max Rigaku system with a rotating anode. The diffractometer was operated at 100 mA and 40 kV with Cu radiation and a graphite monochromator was used to select the Cu $K\alpha_{1,2}$ radiation. Data were collected from $19°$ up to $140°$ with a step size of $0.02°$ and a counting rate of 8 s/step. The structures were refined by the full-pattern method using the program Fulproff [25]. A pseudo-Voigt function was used as the peak shape function and an overall temperature factor was considered.

Magnetic measurements were carried out between 5 K and 300 K by using a commercial quantum design (SQUID) magnetometer. The resistance measurements were performed by the standard four-probe method. Linear thermal expansion measurements were done using the strain-gauge technique [17]. For the resistance and linear thermal expansion measurements, the magnetic field was provided by a 12 T superconducting coil.

3. Results

3.1. X-ray diffraction

All of the $(La_{1-x}Tb_x)_{2/3}Ca_{1/3}MnO_3$ samples have the orthorhombic $GdFeO_3$ structure at room temperature and the crystallographic structure is well described in the space group *Pbnm* (D_{16}^h). This symmetry is the most commonly found one in the related perovskites $REMO_3$ (RE: rare earth; M: transition metal) with orthorhombic distortion [26–28].

With this orthorhombic symmetry, Mn atoms are located at the 4b position: $(\frac{1}{2}\,0\,0)$. From the structural point of view, the absence of superstructure peaks shows indistinct Mn^{3+} and Mn^{4+} positions, indicating a homogeneous mixed-valence state for the manganese ions. The rare-earth or calcium atoms occupy the 4c position: $(x\,y\,\frac{1}{4})$, and the oxygen atoms are in two non-equivalent positions: O(1) at 4c: $(x\,y\,\frac{1}{4})$, and O(2) at 8d: $(x\,y\,z)$.
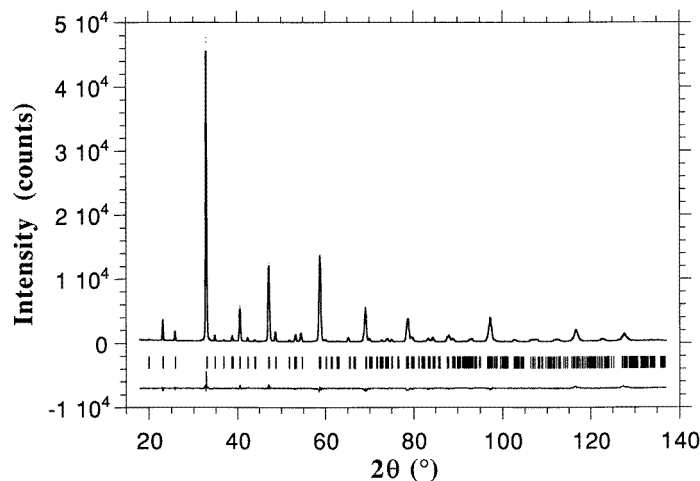

Figure 1. The x-ray powder pattern and best fit (continuous line) at room temperature for $(La_{0.67}Tb_{0.33})_{2/3}Ca_{1/3}MnO_3$. The difference between the experimental and theoretical fits is plotted at the bottom. The bars denote the calculated Bragg-reflected positions.

The structure can be viewed as a distorted ideal cubic perovskite where distortion arises from displacements of oxygen and rare-earth atoms from ideal cubic positions. These displacements are related to a small rare-earth size to support the ideal coordination of
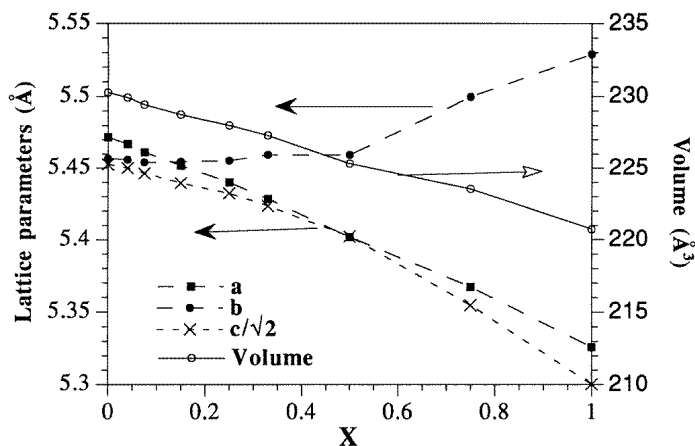
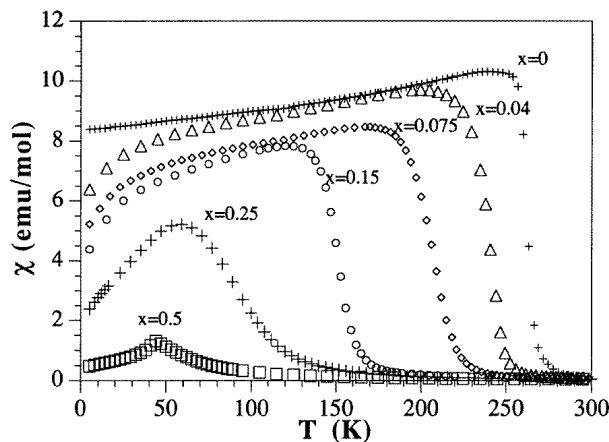**Figure 2.** Lattice parameters and the unit-cell volume of $(La_{1-x}Tb_x)_{2/3}Ca_{1/3}MnO_3$ samples.

Figure 3.   The temperature dependence of the a.c. magnetic susceptibility for selected $(La_{1-x}Tb_x)_{2/3}Ca_{1/3}MnO_3$ samples with $0 \leqslant x \leqslant 0.5$.

12 oxygens. Consequently, the MnO_6 octahedra tilt in order to fill the remaining space. Distortions of the cubic perovskite ABO_3 come from the different ionic radii of the A and B atoms which are related to the Goldsmith tolerance factor [29], defined in our case as

$$t = D_{RE-O}/(\sqrt{2}D_{Mn-O}) \tag{1}$$

where D_{RE-O} is the interatomic distance between the rare-earth (or calcium) and oxygen atoms, and D_{Mn-O} is the interatomic distance between Mn and O atoms. For an ideal cubic perovskite, t is equal to one. As the rare-earth-ion size decreases, the t-value becomes lower. For t slightly less than 1, the octahedra tilt about the threefold axis of the ideal cubic perovskite resulting in a rhombohedral unit cell, as also occurs for $LaNiO_3$ [24]. In our case (lower values of t), the octahedra tilt in phase around $(1\,1\,0)$ and $(0\,0\,1)$ directions of the pseudocubic cell giving an orthorhombic unit cell.

   Figure 1 shows the fitted diffraction pattern for a selected sample. We show the fractional

Table 1. Refined fractional atomic positions, and average Debye–Waller, unit-cell and reliability factors (%) for $(La_{1-x}Tb_x)_{2/3}Ca_{1/3}MnO_3$ at room temperature. The RE (rare-earth and Ca atoms) and O(1) are located at (4c): $(x\ y\ 1/4)$. Mn is at (4b): $(1/2\ 0\ 0)$.

|	x = 0	x = 0.04	x = 0.075	x = 0.15	x = 0.25	x = 0.33	x = 0.5	x = 0.75	x = 1
RE:									
x:	0.9965(2)	0.9955(2)	0.9951(2)	0.9955(3)	0.9939(2)	0.9934(2)	0.9916(2)	0.9910(3)	0.9869(3)
y:	0.0187(1)	0.0201(1)	0.0217(1)	0.0218(1)	0.0270(1)	0.0315(1)	0.0373(1)	0.0487(1)	0.0594(1)
O(1):									
x:	0.0588(14)	0.0631(16)	0.0617(16)	0.0673(19)	0.0688(16)	0.0699(13)	0.0770(13)	0.0912(19)	0.0989(15)
y:	0.4916(8)	0.4897(9)	0.4909(8)	0.4903(10)	0.4878(8)	0.4891(7)	0.4877(9)	0.4743(13)	0.4642(12)
O(2):									
x:	0.7219(11)	0.7216(12)	0.7202(12)	0.7221(14)	0.7183(12)	0.7158(10)	0.7121(10)	0.7139(14)	0.7082(11)
y:	0.2786(11)	0.2793(12)	0.2815(12)	0.2805(13)	0.2865(10)	0.2882(8)	0.2890(8)	0.2887(12)	0.2966(9)
z:	0.0333(6)	0.0307(8)	0.0320(7)	0.0338(9)	0.0340(7)	0.0368(6)	0.0365(6)	0.0433(8)	0.0462(7)
B ($Å^2$):	−0.11(1)	−0.20(1)	0.30 (1)	0.28(1)	0.51(1)	0.84(1)	−0.08(1)	0.35(2)	0.31(2)
a (Å):	5.4717(1)	5.4676(2)	5.4613(1)	5.4517(2)	5.4400(1)	5.4284(1)	5.4018(1)	5.3672(3)	5.3260(2)
b (Å):	5.4569(1)	5.4559(1)	5.4540(1)	5.4544(2)	5.4552(1)	5.4594(1)	5.4595(1)	5.4995(3)	5.5289(3)
c (Å):	7.7112(1)	7.7075(2)	7.7024(1)	7.6927(2)	7.6826(2)	7.6699(1)	7.6400(1)	7.5728(4)	7.4958(3)
R_p:	9.5	8.8	9.5	10.7	9.6	9.0	10.1	13.6	12.8
R_{wp}:	10.8	10.1	10.9	12.0	10.8	9.9	11.0	15.2	14.7
R_{exp}:	5.9	6.0	4.9	5.8	5.3	5.3	6.5	6.1	5.9
χ^2:	3.3	2.8	5.0	4.2	4.1	3.5	2.8	6.1	6.1
R_B:	5.8	5.2	5.5	6.1	5.2	5.2	5.0	6.7	5.0

coordinates, unit cell and conventional Rietveld reliability factors in table 1. The low values of the reliability factors confirm the accuracy of the chosen structural model. Table 2 shows the interatomic distances and angles for MnO_6 octahedra from refined atomic positions.

The evolution of the cell volume and lattice parameters are displayed in figure 2. The continuous unit-cell-volume decrease along the series is due to the smaller size of the Tb^{3+} [30], this reduction being of about 4% when the substitution for La of Tb is complete ($x = 1$). While a and c decrease continuously with the Tb concentration, the parameter b does not change with the Tb concentration for $x \leqslant 0.5$ and shows an increase for higher Tb concentrations as can be seen in figure 2 and table 1. This change in the behaviour of parameter b is characteristic of perovskites with high orthorhombic distortion, such as occurs in orthoferrites [31]. Therefore $a > b \approx c/\sqrt{2}$ for $La_{2/3}Ca_{1/3}MnO_3$ and samples with low Tb concentration showing a slight orthorhombic distortion, while $b > a > c/\sqrt{2}$ for $Tb_{2/3}Ca_{1/3}MnO_3$, with higher orthorhombic distortion.

Another important aspect of this structural study is the configuration of the MnO_6 octahedron through the series. As can be seen in table 2, the angles O–Mn–O are very close to 90°, which is expected for a regular octahedron, and the three Mn–O distances are very similar over the whole series, showing no static Jahn–Teller distortion. Taking into account the values of ionic radii [30] and that Mn^{3+} is a Jahn–Teller ion, these distances are more in agreement with the same oxidation state of Mn (33% of Mn^{4+} and 67% of Mn^{3+}) for the whole series. The decrease in t (increase in Tb) leads to a decrease in the Mn–O–Mn angle which, as we will discuss below, is a key factor that controls the Mn–Mn electronic hopping.

Table 2. Interatomic distances (Å) and angles (deg) for the Mn–O octahedron of $(La_{1-x}Tb_x)_{2/3}Ca_{1/3}MnO_3$ at room temperature.

	No	$x = 0$	$x = 0.04$	$x = 0.075$	$x = 0.15$	$x = 0.25$	$x = 0.33$	$x = 0.5$	$x = 0.75$	$x = 1$
Mn–O(1):										
	2	1.955(1)	1.958(1)	1.956(1)	1.959(2)	1.958(2)	1.956(1)	1.956(1)	1.961(3)	1.957(2)
Mn–O(2):										
	2	1.963(6)	1.961(6)	1.966(6)	1.969(7)	1.980(6)	1.982(4)	1.969(5)	1.987(7)	2.009(5)
	2	1.959(6)	1.955(7)	1.953(7)	1.948(8)	1.942(6)	1.948(5)	1.955(5)	1.953(7)	1.949(5)
⟨Mn–O⟩:		1.959	1.958	1.958	1.958	1.960	1.962	1.960	1.976	1.979
Mn–Mn:										
	2	3.855(1)	3.854(1)	3.851(1)	3.846(1)	3.841(1)	3.835(1)	3.820(1)	3.786(1)	3.748(1)
	4	3.864(1)	3.862(1)	3.859(1)	3.856(1)	3.852(1)	3.849(1)	3.840(1)	3.842(1)	3.838(1)
O(1)–Mn–O(2):										
	2	90.9(3)	90.7(4)	90.3(3)	90.4(5)	90.7(4)	90.3(2)	90.7(3)	92.4(4)	93.8(3)
	2	90.5(4)	90.0(4)	90.1(4)	90.1(4)	90.1(4)	90.1(3)	90.5(3)	90.5(4)	90.8(3)
	2	89.5(4)	90.0(4)	89.9(3)	89.9(5)	89.9(4)	89.9(2)	89.5(2)	89.5(5)	89.2(4)
	2	89.1(4)	89.3(4)	89.7(4)	89.6(4)	89.3(3)	89.7(3)	89.3(2)	87.6(3)	86.2(3)
O(2)–Mn–O(2):										
	2	91.1(4)	90.9(4)	91.1(5)	91.0(5)	91.0(4)	91.0(3)	90.6(4)	90.4(5)	90.0(4)
	2	88.9(4)	89.1(4)	88.9(4)	89.0(5)	89.0(4)	89.0(3)	89.4(3)	89.6(4)	90.0(4)
Mn–O(1)–Mn:										
	2	160.9(3)	159.4(3)	159.9(3)	158.2(4)	157.6(3)	157.3(3)	155.1(3)	149.9(4)	146.6(3)
Mn–O(2)–Mn:										
	4	160.4(14)	160.8(10)	159.9(15)	159.8(18)	158.2(13)	156.7(9)	156.1(9)	154.4(13)	151.6(8)
⟨Mn–O–Mn⟩:		160.6	160.3	159.9	159.2	158.0	156.9	155.8	152.9	149.9
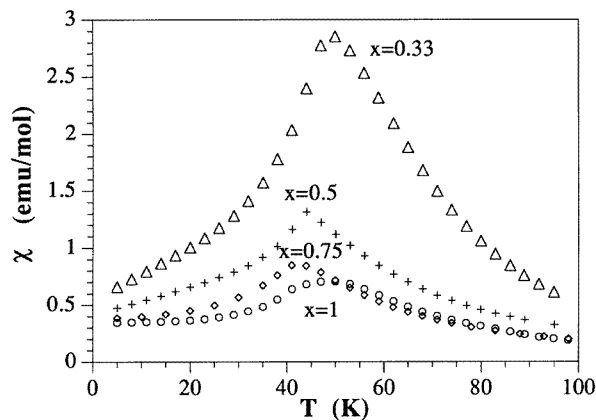
Figure 4. The temperature dependence of the a.c. magnetic susceptibility of the $(La_{1-x}Tb_x)_{2/3}Ca_{1/3}MnO_3$ samples with $0.33 \leqslant x \leqslant 1$.

3.2. Magnetic properties

a.c. initial magnetic susceptibility measurements of the series $(La_{1-x}Tb_x)_{2/3}Ca_{1/3}MnO_3$ as a function of temperature are shown in figures 3 and 4. The susceptibility behaviour allows
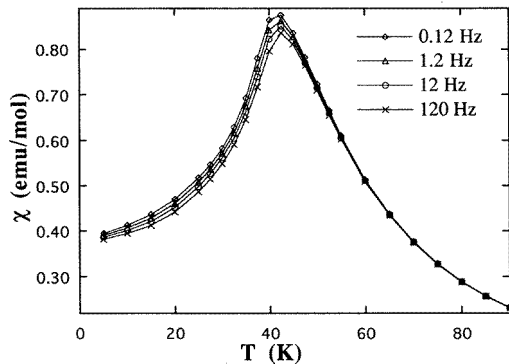
Figure 5. Thermal dependences of the a.c. magnetic susceptibility of $(La_{0.5}Tb_{0.5})_{2/3}Ca_{1/3}MnO_3$ samples at different frequencies of the magnetic excitation field (4.5 Oe).
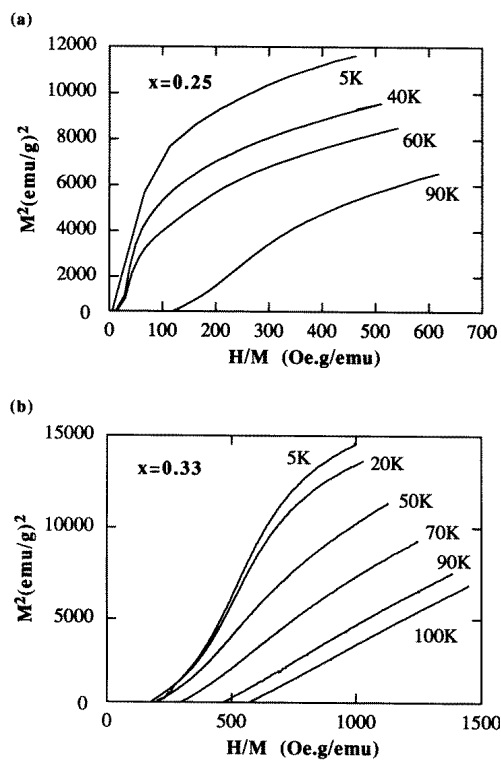

Figure 6. Arrott's plots for $(La_{1-x}Tb_x)_{2/3}Ca_{1/3}MnO_3$ samples with $x = 0.25$ and $x = 0.33$.

one to distinguish two different regions depending on the Tb content. The susceptibility curves of samples with $x < 0.33$ show a sharp jump corresponding to the ferromagnetic–paramagnetic phase transition. The Curie temperature, defined as the inflexion point of the susceptibility curves, decreases with the Tb content in the samples. Magnetization curves of these samples show net magnetic moments such as occur in the parent $La_{2/3}Ca_{1/3}MnO_3$ sample. At $x \geqslant 0.33$, the sharp jump of the ferromagnetic order disappears and a peak

anomaly appears at around 50 K. Figure 5 shows the frequency dependence of the a.c. initial magnetic susceptibility peak for the $x = 0.5$ sample. The cusp shifts towards lower temperatures and there is an intensity increase as the frequency of the a.c. field decreases in agreement with a spin-glass behaviour. Similar results have been found for samples with $x \geqslant 0.33$. Figure 6 shows the Arrott plots for $x = 0.25$ and $x = 0.33$. These plots clearly show that $x = 0.25$ is ferromagnetic below $T_c \approx 103$ K. However, the lack of spontaneous magnetization in the $x = 0.33$ compound indicates the absence of long-range magnetic order. This result agrees with a recent neutron diffraction study of the $x = 0.33$ sample which has showed the absence of long-range ferromagnetic interactions and strong short-range magnetic correlations [32]. The boundary between long-range ferromagnetism and spin glass can be established as lying at around $x = 0.33$. This spin-glass behaviour can arise from competitive antiferromagnetic (via superexchange) and ferromagnetic interactions (via double exchange). This kind of competition has already been seen in these systems [33].
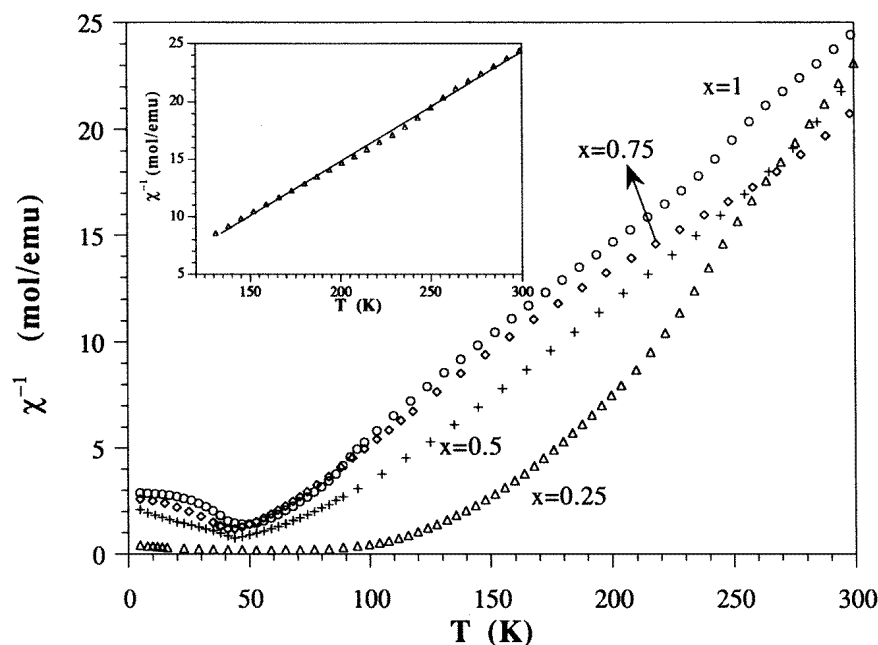

Figure 7. The inverse of the magnetic susceptibility versus temperature for selected $(La_{1-x}Tb_x)_{2/3}Ca_{1/3}MnO_3$ samples. The inset shows the Curie–Weiss behaviour of a $Tb_{2/3}Ca_{1/3}MnO_3$ sample.

Moreover, only the $Tb_{2/3}Ca_{1/3}MnO_3$ sample obeys a Curie–Weiss law at temperatures higher than 150 K. The fit of the susceptibility curve for this sample to the equation

$$\chi = C/(T - \theta_c) \tag{2}$$

gives the following values: $C = 10.65$ emu K mol^{-1}, $\theta_c = 41.5$ K. This value of θ_c correlates quite well with the maximum in the susceptibility curve indicating the presence of ferromagnetic correlations. On the other hand, the calculated paramagnetic effective magnetic moment is $\mu_{eff} = 9.23$ μ_B, which correlates very well with the theoretical value, calculated as

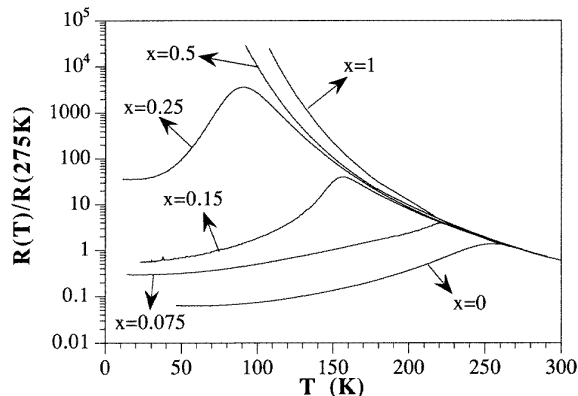$$\mu_t = \sqrt{0.67\mu^2_{Tb^{3+}} + 0.33\mu^2_{Mn^{4+}} + 0.67\mu^2_{Mn^{3+}}} = 9.16 \ \mu_B$$

Figure 8. Resistance versus temperature for selected $(La_{1-x}Tb_x)_{2/3}Ca_{1/3}MnO_3$ samples. The data have been normalized to the resistance at 275 K.

taking 9.5 μ_B, 3.8 μ_B and 4.9 μ_B as the effective magnetic moments for Tb^{3+}, Mn^{4+} and Mn^{3+} respectively [34]. This result agrees with all Tb as $+3$ and the same ratio Mn^{4+}: Mn^{3+} for the whole series.
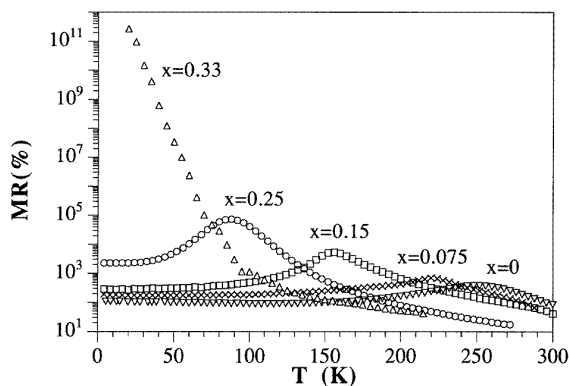

Figure 9. Magnetoresistance versus temperature for selected $(La_{1-x}Tb_x)_{2/3}Ca_{1/3}MnO_3$ samples.

The other samples of the series do not follow a Curie–Weiss law as can be seen in figure 7. This feature can be related to large magnetic correlations at temperatures higher than T_c as has been observed by neutron diffraction [35].

3.3. Electrical properties

Resistance versus temperature curves are displayed in figure 8 for selected samples without external magnetic fields. Samples with low Tb content ($x < 0.33$) show a peak in their resistance curves at the Curie temperature. Therefore, as the Tb content increases, the maximum of resistance increases and the peak appears at lower temperatures [36]. Similar results have been reported for the $(La_{1-x}Pr_x)_{2/3}Ca_{1/3}MnO_3$ system [12]. Samples with high contents of Tb ($x \geqslant 0.33$) show a semiconducting-type resistance up to the saturation of our experimental set-up. Using an appropriate set-up, the resistivity of the $x = 0.33$

sample showed a value of $\rho = 10^{13}$ Ω cm at 20 K. This sample does not show long-range ferromagnetic ordering as we have shown before. Nevertheless the resistances of the samples are also affected by the presence of an external magnetic field. Figure 9 shows the MR of selected samples. We here define magnetoresistance as

$$\mathrm{MR}(\%) = \frac{|R(H = 12\ \mathrm{T}) - R(H = 0)|}{R(H = 12\ \mathrm{T})} \times 100. \tag{3}$$

The replacement of La by Tb results in an overall rise in the peak (negative) of magnetoresistance together with a downward shift in temperature. For $x = 0.33$ there is no MR peak due to its semiconducting behaviour over the whole temperature range, but it shows the largest MR effects at low temperatures. This result makes evident the strong magnetic correlations of conduction carriers even in samples without long-range ferromagnetic ordering.
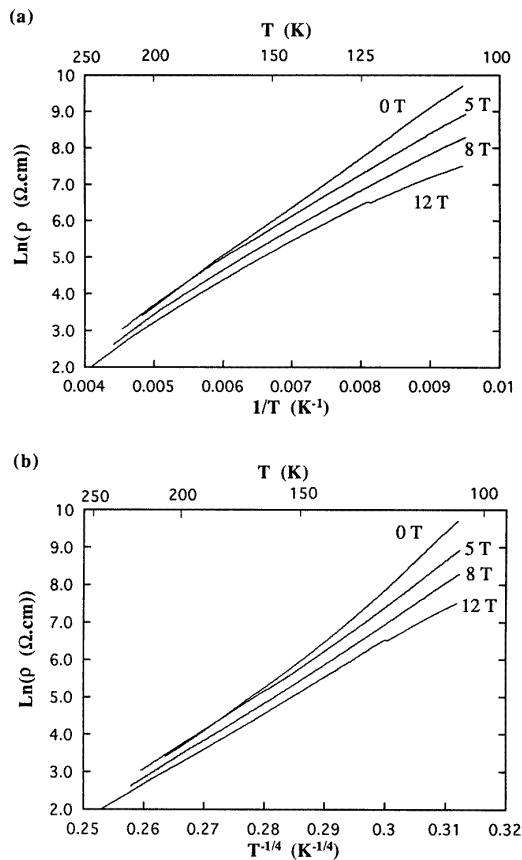

Figure 10. (a) ln ρ versus $1/T$ and (b) ln ρ versus $1/T^{1/4}$ for $(\mathrm{La}_{0.67}\mathrm{Tb}_{0.33})_{2/3}\mathrm{Ca}_{1/3}\mathrm{MnO}_3$ at several external magnetic fields.

The resistivity can be fitted to Mott's law as well as an Arrhenius law at temperatures above T_c for samples with ferromagnetic ordering. There are no clear reasons for choosing one of them and this feature could be related to the high rise of the resistivity above T_c together with the small range of temperatures studied. For samples without ferromagnetic

ordering (or high Tb content) the resistivity without external magnetic fields fits better to an Arrhenius law than to Mott's law. The values of activation energies (E_a) obtained for the whole $(La_{1-x}\ Tb_x)_{2/3}Ca_{1/3}MnO_3$ series range between 0.12 eV and 0.16 eV showing a slight increase with the Tb content in the sample. Similar values of E_a have been obtained recently for $La_{1-x}Ca_xMnO_3$ pellets [37] and $La_{1-x}Sr_xMnO_z$ films [9].
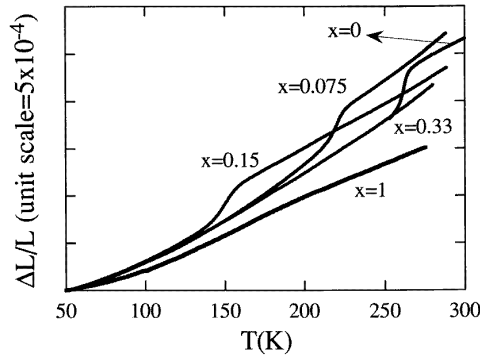

Figure 11. Linear thermal expansion for selected $(La_{1-x}Tb_x)_{2/3}Ca_{1/3}MnO_3$ samples.

On the other hand, E_a decreases for all samples on applying an external magnetic field. This fact must be related to a diminution of the energy gap due to a lower hopping energy for the carriers. For samples with ferromagnetic ordering, the magnetic field induces the metallic state which is manifested by a diminution of the peak [36], while for samples with high Tb content (not ferromagnetic) we have observed a change in the conduction mechanism. This feature can be seen in figure 10 for the $x = 0.33$ sample. While the resistance of this sample follows an Arrhenius law at zero field, the straight line bends when an external magnetic field is applied (see figure 10(a)) and now the resistance follows Mott's law (see figure 10(b)).

3.4. Thermal expansion

Linear thermal expansion curves reported in figure 11 show different behaviours depending on the Tb content. At low x-values the thermal expansion shows a discontinuity which coincides with the metal–semiconductor phase transition. This result, as has been observed for other doped samples [17], clearly demonstrates that associated with the magnetic ordering and electronic localization there is a lattice effect. In other words, magnetoelastic coupling plays an important role in this phenomenon. The other point that we would like to stress is that the spontaneous transition to the metallic state disappears exactly at the concentration at which no long-range ordering occurs.

In order to study the effect of the magnetic field in the linear thermal expansion, we have measured the linear thermal expansion under a steady field of up to 12 T. Figures 12(a) and 12(b) show these effects for two representative samples. As is observed in figure 12(a) for $x = 0.15$, the effect of the field is to suppress the carrier localization above T_c and below T_p (the localization temperature) [17]. This result, as for the yttrium-doped sample, shows a tight connection between magnetoelastic and magneto-transport properties indicating a strong electron–phonon coupling. Figure 12(b) shows the field effect for $x = 1$, which is different from that for the ferromagnetic samples. Magnetostriction measurements of this sample at different external magnetic fields show a linear and positive behaviour, opposite
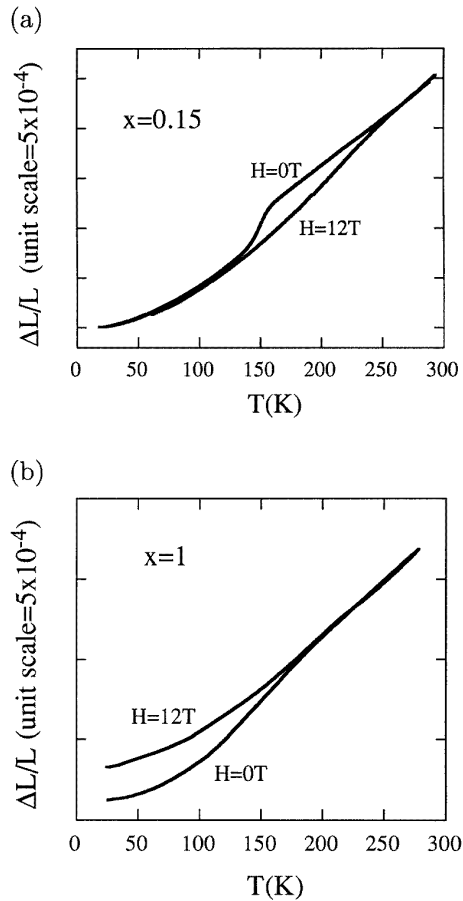
(a)

(b)

Figure 12. Linear thermal expansion of (a) $(La_{0.85}Tb_{0.15})_{2/3}Ca_{1/3}MnO_3$ and (b) $Tb_{2/3}Ca_{1/3}MnO_3$ samples at zero field and under an external field of 12 T.

to the features observed for $x < 0.33$ samples [38]. This behaviour is not well understood yet.

4. Discussion

Several relevant points regarding the occurrence of giant magnetoresistance in manganese oxide perovskites and the mechanisms which control the simultaneity of ferromagnetism and metallic conduction can be obtained from the present study.

The first point is the correlation between crystallographic structure and the metal–semiconductor phase transition. Our results show that the substitution for La with Tb induces the lowering of the Curie temperature. For concentrations higher than $x = 0.33$, this transition disappears, giving rise to spin-glass behaviour. Two structural effects occur when La is replaced by Tb:

(i) the decrease in the volume cell due to the lower ionic radius of Tb^{3+};
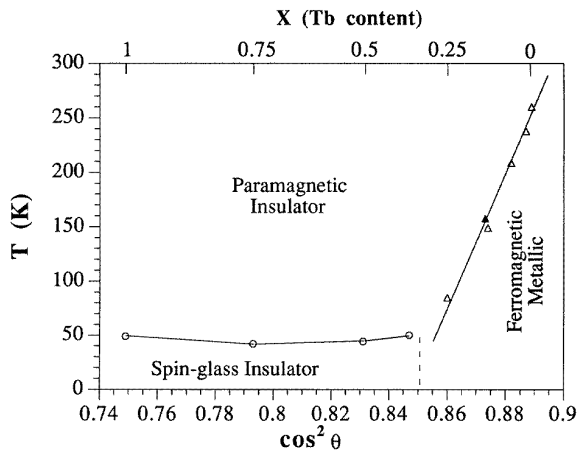(ii) the decrease in the Mn–O–Mn bond angle with the Tb content.

Figure 13. The phase diagram of the $(La_{1-x}Tb_x)_{2/3}Ca_{1/3}MnO_3$ series as a function of the Mn–O–Mn angle. White triangles indicate T_c for samples with $x \leqslant 0.25$ (see the top of the figure), while the black triangle indicates T_c for the $La_{0.6}Y_{0.07}Ca_{1/3}MnO_3$ sample [17]. Circles indicate the temperature of the cusp peak (a.c. susceptibility at 12 Hz) for samples with $x \geqslant 0.33$. The lines are guides for the eyes.

Previous interpretations suggested that an increase in the 'chemical pressure' induces a drop in the Curie temperature with an increase in the magnetoresistance [14]. This interpretation contradicts recent experiments on the effects of pressure on $La_{0.6}Y_{0.07}Ca_{0.33}MnO_3$ which indicate an increase in T_c and a decrease in the magnetoresistance on applying hydrostatic pressure [15]. These results are in agreement with the expected pressure-enhanced double-exchange interaction due to the shortening of the Mn–Mn distance. This apparent controversy can be solved as has been reported for the $(La_{1-x}Pr_x)_{0.7}Ca_{0.3}MnO_3$ system [12]. The authors of [12] proposed that the tolerance factor (see equation (1) in section 3.1) is the key which controls the Curie temperature and the occurrence of magnetoresistance. They proposed a universal phase diagram which correlates the tolerance factor with the Curie temperature for $A_{0.7}B_{0.3}MnO_3$ systems. Our results coincide with this diagram and confirm that the ionic radius of the trivalent metal is the parameter which controls the existence of ferromagnetism. The main structural effect of decreasing the rare-earth radius in these systems is the diminution in the Mn–O–Mn angle which brings about the shifting of the metal–insulator phase transition towards lower temperatures as has been proposed for related nickel oxides [39]. Similar results were obtained in the past for orthoferrites where a linear dependence of T_N on $\cos^2 \theta$ (where θ is the Fe–O–Fe angle) was obtained [40]. This result has been explained on the basis of antiferromagnetic ordering due to superexchange interactions whose strength varies as $\cos^2 \theta$ [41].

In figure 13 we have plotted T_c for the samples studied versus $\cos^2 \theta$ (θ = Mn–O–Mn angle) obtaining a straight line, as also occurs in the case of superexchange for orthoferrites. The $(La_{1-x}Tb_x)_{2/3}Ca_{1/3}MnO_3$ samples have as a common feature the same orthorhombic structure and a tolerance factor value (t) ranging between 0.92 and 0.89, and, say, a Mn–O–Mn angle from $160.6°$ down to $149.9°$. For higher angles, such as occur in the $(La, Y)_{2/3}Sr_{1/3}MnO_3$ series [12], T_c reaches a maximum value ($\langle Mn–O–Mn \rangle = 166.3°$, $T_c \approx 360$ K), which coincides with the change from an orthorhombic to a rhombohedral cell, followed by a decrease in T_c for higher values of this angle. The decrease in T_c for

the rhombohedral samples has been attributed to the competition with the antiferromagnetic superexchange interaction whose strength is increased with the angle [41]. From our results, we can establish a low-angle limit where the weakness of the ferromagnetic double-exchange interaction competes again with the antiferromagnetic superexchange interaction resulting in a low-temperature spin-glass state. This limit, marked by the sample with $x = 0.33$, which is already a spin glass at low temperatures [32], corresponds to an average angle of $157°$. On the other hand, for the range between $160.6°$ and $157°$, the reduction in the ferromagnetic double-exchange interaction produces the linear reduction in T_c as is observed in figure 13.

In order to explain the origin of the dependence of the physical properties on the Mn–O–Mn angle, it is necessary to know the electronic structure of these oxides. In the past, it was assumed that substitution for La with M^{2+} produces the oxidation of Mn^{3+} (d^4) to Mn^{4+} (d^3) and allows control of the oxidation state of the Mn sublattice [1–5]. However, recent studies on Mn 2p and O 1s absorption spectra of $La_{1-x}Sr_xMnO_3$ concluded that the holes induced by substitution in this series go to states of mixed character: $3d^3 + 3d^4L$, where L is a hole in the O 2p band [42]. Similar results have been obtained in XPS experiments, establishing [43] that the double-exchange mechanism in the metallic phase is caused by the itinerant holes doped into $LaMnO_3$ of mainly oxygen p character with e_g symmetry and, consequently, these holes are coupled with d^4 local moments of Mn^{3+} ions and align with them ferromagnetically.

Taking into account these precedents, we can justify the results obtained on the $(La_{1-x}Tb_x)_{2/3}Ca_{1/3}MnO_3$ series as follows. The diminution of the Mn–O–Mn angles leads to a decrease in the electron hopping between Mn sites resulting in a decrease in the double-exchange interaction. This may be due to a reduction in the conduction bandwidth and the electron transfer between the Mn 3d and O 2p orbitals. This effect produces the decrease in T_c and the increase in the activation energy of the semiconductor phase.

Another point that we want to stress is that for higher Tb doping levels, the competition between superexchange and double exchange leads to the formation of a spin-glass phase at low temperatures. In this series, the absence of insulating ferromagnetism indicates that ferromagnetism coupling is driven by hopping of electrons between different manganese atoms, and in consequence ferromagnetism and metallic conduction have as their origins the same interaction, the so-called 'double-exchange interaction' [7, 8].

The third important point to be underlined is the simultaneous presence of a volume discontinuity at the ferromagnetic transition and the large magnetoelastic effects observed for these compounds. A theoretical calculation using a simplified double-exchange Hamiltonian of the magnetic-field-dependent resistivity near the transition temperature showed the inconsistency with the experimental results and the authors proposed that a large electron–phonon coupling may play an important role [19]. The behaviour of the linear thermal expansion is the experimental evidence of such a coupling. The detailed analysis of the thermal expansion of the yttrium-doped $LaCaMnO_3$ perovskites shows that the thermal expansion differs from the normal phonon anharmonic contribution, given by the Grüneisen law, below a temperature T_p well above T_c. This feature indicates that the gradual electronic localization produces a local distortion as the temperature decreases, and the sharp jump of $\Delta l/l$ at T_c can be explained as being a consequence of the electronic delocalization. This is also supported by x-ray absorption experiments at the Mn K edge in $La_{2/3}Ca_{1/3}MnO_3$, which have recently demonstrated the presence of local distortion well above T_c that disappears below T_c [44].

The suppression of the anomaly in the thermal expansion by the presence of an external field correlates with the resistivity measurements and may give a picture of the mechanism

of this phenomenon. In the paramagnetic phase, the electronic localization produces an anomalous volume contribution above T_c ($T_p \approx 1.8$ T_c) showing short-range magnetic order as has been observed by using neutron diffraction techniques [35]. These magnetic interactions would explain the absence of a Curie–Weiss behaviour in the χ_{ac}-curves (see figure 7). In the presence of a magnetic field the strong spin–spin correlations are enhanced, giving rise to an alignment of the Mn magnetic moments. As a consequence of the double-exchange interaction, carrier localization is not possible and the extra volume contribution is suppressed [17]. Below T_c, the long-range magnetic order is responsible for the electrical conductivity through the double-exchange interaction and the lattice distortion is spontaneously suppressed. The close correlation between magnetization and electrical resistivity has also been manifested by recent transport and magnetic measurements [45].

5. Conclusions

The $(La_{1-x}Tb_x)_{2/3}Ca_{1/3}MnO_3$ system has been exhaustively studied, clarifying important points in the description of the mixed-valence oxide manganese perovskites with giant magnetoresistance.

The oxidation state of the Mn sublattice remains unchanged over the whole series and all samples show an orthorhombic unit cell whose main crystallographic difference is the decrease in the Mn–O–Mn angle with increasing Tb content. This decrease gives rise to a diminution of T_c and an increase in the giant magnetoresistance. Our study has indicated that the double-exchange interaction, responsible for the metallic behaviour and ferromagnetic ordering, depends on the Mn–O–Mn angle. A limit value has been established for this angle ($\theta \approx 157°$), where the competition between superexchange and double exchange leads to the formation of a spin glass. The formation of a spin-glass state instead of a ferromagnetic insulator state shows the high correlation between ferromagnetism and metallic conduction for this carrier concentration.

Thermal expansion results have allowed us to propose the existence of two different conduction mechanisms above and below T_c. At high temperatures the conduction is polaronic-like and the charge localization produces local distortion of the lattice. The effect of an external magnetic field is to align the spins and to suppress the local distortions. At low temperatures conduction is due to electronic hopping between different Mn atoms via the double-exchange interaction. In any case, the theory of the double-exchange interaction needs to be developed in order to describe the variation of the strength as a function of the Mn–O–Mn angle. The dependence of the transfer integral between the O 2p and Mn 3d wave functions with the angle must be the origin of the high dependence of the interaction strength on the Mn–O–Mn angle.

References

[1] Jonker G H and Van Santen J H 1950 *Physica* **16** 337
[2] Goodenough J B 1955 *Phys. Rev.* **100** 564
[3] Jonker G H 1956 *Physica* **22** 707
[4] Goodenough J B, Wold A, Arnott R J and Menyuk N 1961 *Phys. Rev.* **124** 373

  [5] Matsumoto G 1970 *J. Phys. Soc. Japan* **29** 606
  [6] Wollan E O and Koehler W C 1955 *Phys. Rev.* **100** 545
  [7] Zener C 1951 *Phys. Rev.* B **82** 403
  [8] de Gennes P G 1960 *Phys. Rev.* **118** 141
  [9] Ju H L, Kwon C, Li Q, Greene R L and Venkatesan T 1994 *Appl. Phys. Lett.* **65** 2108
 [10] Mahendiran P, Raychaudhuri A K, Chainani A, Sarma D D and Roy S B 1995 *Appl. Phys. Lett.* **66** 233
 [11] Xiong G C, Li Q, Tiefel T H, Fleming R M and Philipy J M 1995 *Appl. Phys. Lett.* **66** 1427
 [12] Hwang H Y, Cheong S W, Radaelli P G, Marezio M and Batlogg B 1995 *Phys. Rev. Lett.* **75** 914
 [13] Raveau B, Maignan A and Caignaert V 1995 *J. Solid State Chem.* **117** 424
 [14] Jin S, O'Bryan H M, Tiefel T H, McCormack M and Rhodes W W 1995 *Appl. Phys. Lett.* **66** 382
 [15] Arnold Z, Kamenev K, Ibarra M R, Algarabel P A, Marquina C, Blasco J and García J 1995 *Appl. Phys. Lett.* **67** 2875
 [16] Morimoto Y, Asamitsu A and Yokura Y 1995 *Phys. Rev.* B **51** 16 491
 [17] Ibarra M R, Algarabel P A, Marquina C, Blasco J and García J 1995 *Phys. Rev. Lett.* **75** 3541
 [18] Radaelli P G, Cox D E, Marezio M, Cheong S-W, Schiffer P E and Ramirez A P 1995 *Phys. Rev. Lett.* **75** 4488
 [19] Millis A J, Litlewood P B and Shraiman B I 1995 *Phys. Rev. Lett.* **74** 5144
 [20] Kobayashi T, Takizawa H, Endo T, Sato T, Shimada M, Taguchi H and Nagao M 1991 *J. Solid State Chem.* **92** 116
 [21] Yakel H L, Koehler W C, Bertaut E F and Forrat E F 1963 *Acta Crystallogr.* **16** 957
 [22] Giaquinta D M and Zur Loye H C 1994 *Chem. Mater.* **6** 365
 [23] Blasco J, Castro M and García J 1994 *J. Phys.: Condens. Matter* **6** 5875
 [24] Gushee B E, Katz L and Ward R 1957 *J. Am. Chem. Soc.* **79** 5601
 [25] Rodríguez-Carvajal J L and Pannetier M A 1987 *ILL Report* 87TR014T
 [26] García-Muñoz J L, Rodríguez-Carvajal J, Lacorre P and Torrance J B 1992 *Phys. Rev.* B **46** 4414
 [27] Liu S and Prewitt C T 1991 *J. Phys. Chem. Solids* **52** 441
 [28] Geller S 1957 *Acta Crystallogr.* **10** 243
 [29] Goldsmith V M 1927, 1928 *Geochemische Verteilungsgesetze der Elemente VII–VIII*
 [30] Shannon R D 1976 *Acta Crystallogr.* A **32** 751
 [31] Robbins M, Pierce R D and Wolfe R 1971 *J. Phys. Chem. Solids* **32** 1789
 [32] de Teresa J M, Ibarra M R, García J, Blasco J, Ritter C, Algarabel P, Marquina C and del Moral A 1996 *Phys. Rev. Lett.* **76** 3392
 [33] Troyanchuk I O and Pastushonok S N 1989 *Phys. Status Solidi* **115** K225
 [34] Cheetham A K and Day P 1987 *Solid State Chemistry: Techniques* (Oxford: Oxford University Press) pp 135–7
 [35] de Teresa J M, Ibarra M R, Blasco J, García J, Marquina C, Algarabel P A, Arnold Z, Kamenev K, Ritter C and von Helmolt R 1996 *Phys. Rev.* B **54** 1187
 [36] de Teresa J M, Blasco J, Ibarra M R, García J, Marquina C, Algarabel P A and del Moral A 1995 *Solid State Commun.* **96** 627
 [37] Mahendiran R, Malesh R, Raychaudhuri A K and Rao C N 1995 *Solid State Commun.* **94** 515
 [38] de Teresa J M, Blasco J, Ibarra M R, García J, Marquina C, Algarabel P A and del Moral A 1996 *J. Appl. Phys.* **79** 5175
 [39] Blasco J and García J 1994 *J. Phys.: Condens. Matter* **6** 10 759
 [40] Treves D, Eibschütz M and Coppens P 1965 *Phys. Lett.* **18** 216
 [41] Sawatzky G A, Geertsma W and Haas C 1976 *J. Magn. Magn. Mater.* **3** 37
 [42] Abbate M, de Groot F M F, Fuggle J C, Fujimori A, Strebel O, Lopez F, Domke M, Kaindl G, Sawatzky G A, Takano M, Takeda Y, Eisaki H and Uchida S 1992 *Phys. Rev.* B **46** 4511
 [43] Saitoh T, Bocquet A E, Mizokawa T, Namatame H, Fujimori A, Abbate M, Takeda Y and Takano M 1995 *Phys. Rev.* B **51** 13 942
 [44] Tyson T A, Mustre de Leon J, Conradson S D, Bishop A R, Neumeier J J and Zang J 1996 *Phys. Rev. Lett.* submitted
 [45] Hundley M F, Hawlay M, Heffner R H, Jia Q X, Neumeier J J, Tesmer J, Thompson J D and Wu X D 1995 *Appl. Phys. Lett.* **67** 860